PHYSICS

Characterizing many-body dynamics with projected ensembles on a superconducting quantum processor

Zhiguang Yan[1]*†, Zi-Yong Ge[1]*†, Rui Li[1], Yu-Ran Zhang[2], Franco Nori[1,3], Yasunobu Nakamura[1,4]

Quantum simulators allow the experimental exploration of nonequilibrium quantum many-body dynamics, which have traditionally been characterized through expectation values or entanglement measures, based on density matrices of the system. Recently, a more general framework for studying quantum many-body systems based on projected ensembles has been introduced, revealing quantum phenomena, such as deep thermalization in chaotic systems. Here, we experimentally investigate a chaotic quantum many-body system using projected ensembles on a three-dimensional–integrated frequency-tunable superconducting processor, enabling both high-fidelity control and scalable architecture. Our results provide direct evidence of deep thermalization by observing a Haar-distributed projected ensemble for the steady states within a charge-conserved sector. Moreover, by introducing an ensemble-averaged entropy as a metric, we establish a benchmark for many-body information leakage from the system to its environment. Our work paves the way for studying quantum many-body dynamics using projected ensembles, and the scalability of our benchmark method represents a notable advance toward quantum computation and simulation.

INTRODUCTION

Understanding the nonequilibrium dynamics of closed quantum many-body systems (*1*) remains a central challenge in modern quantum physics. Recent advances in quantum simulations (*2*–*4*) have provided powerful experimental platforms to explore this problem in depth. It has been shown that isolated chaotic systems, initialized in typical pure states, can evolve toward thermal equilibrium, where the reduced density matrix of a local subsystem resembles a Gibbs ensemble (*5*–*11*). This process, known as quantum thermalization, is well described by the Eigenstate Thermalization Hypothesis (*7*). However, reduced density matrices capture only limited information, notably lacking access to higher-order moments of the quantum ensemble. To address this limitation, the concept of projected ensembles has recently been introduced (*12*–*15*), providing a more complete characterization of quantum thermalization. A projected ensemble is constructed by performing projective measurements on the complementary subsystem in a fixed local basis, yielding a collection of postmeasurement wave functions on the subsystem of interest. Thus, projected ensembles retain full information about the many-body wave function and can uncover universal properties beyond what is accessible only through reduced density matrices. In particular, in certain chaotic systems, projected ensembles can exhibit the emergence of quantum state designs (*16*, *17*) after long-time evolution, a phenomenon known as deep thermalization (*12*–*14*), which is a stronger form of quantum thermalization. Despite its theoretical importance, direct experimental observation of deep thermalization has remained elusive.

In quantum simulations, another fundamental concern is evaluating how well a quantum system remains isolated from its environment, which requires quantifying its information leakage. Conventionally, the single-qubit energy relaxation time T_1 and dephasing time T_2^* are used to characterize the coupling strength to the environment. However, T_1 and T_2^* are insufficient to accurately capture information leakage in many-body regimes. For example, it has been shown that dephasing can be suppressed when all qubits in a superconducting circuit are tuned to resonance (*18*). A general approach to quantify quantum information leakage is through entropy measures, which are extremely challenging to access in quantum many-body systems (*19*–*22*). This highlights the need for scalable methods to benchmark many-body information leakage in quantum simulators. While measuring the full projected ensemble still remains experimentally difficult, to study a subset of high-probability states within the projected ensemble is accessible for experiments. This reduced ensemble still encodes substantial global information about the underlying quantum many-body wave function. These considerations naturally lead to an intriguing question: Can projected ensembles offer a practical and scalable approach to benchmarking many-body information leakage in quantum simulators?

In this work, by using a three-dimensional (3D)–integrated frequency-tunable superconducting quantum processor with high-fidelity control and scalable architecture, we experimentally investigate the dynamics of a quantum many-body system from the perspective of projected ensembles. The effective Hamiltonian of the system is described by a 2D spin-$\frac{1}{2}$ XY model, exhibiting spin $U(1)$ symmetry. Focusing on a subsystem of two nearest-neighbor qubits, we explore deep thermalization starting from a half-filling product state. After a long-time evolution, the projected ensemble within the spin-conserved sector exhibits a Haar-random distribution, providing direct experimental evidence of deep thermalization. Furthermore, by using ensemble-averaged entropies of projected ensembles, we benchmark many-body information leakage, which can hardly be captured by single-qubit decoherence measurements. Our results highlight the power of projected ensembles in characterizing quantum many-body dynamics, offering insights beyond conventional observables based on density matrices.

RESULTS

Projected ensembles and experimental setup

We begin by briefly reviewing the concept of projected ensembles. We partition a quantum many-body system into two parts: a local

[1]Center for Quantum Computing (RQC), RIKEN, Wako, Saitama 351-0198, Japan. [2]School of Physics and Optoelectronics, South China University of Technology, Guangzhou 510640, China. [3]Department of Physics, University of Michigan, Ann Arbor, MI 48109-1040, USA. [4]Department of Applied Physics, Graduate School of Engineering, The University of Tokyo, Bunkyo-ku, Tokyo 113-8656, Japan.
*Corresponding author. Email: marzgy09@gmail.com (Z.Y.); ziyong.ge@riken.jp (Z.-Y.G.)
†These authors contributed equally to this work.

subsystem A and its complement B. For a quantum state $|\Psi\rangle$, the wave function can be expressed as: $|\Psi\rangle = \sum_{z_B} \sqrt{p(z_B)}\,|\Psi_A(z_B)\rangle \otimes |z_B\rangle$, where $|z_B\rangle$ is a measurement basis for B (represented as a bit-string in our experiment), $p(z_B)$ is the probability of measuring the bit-string z_B, and $|\Psi_A(z_B)\rangle$ is the resulting state of A when B collapses to $|z_B\rangle$ (Fig. 1A). The projected ensemble of subsystem A with respect to $|\Psi\rangle$ is then defined as

$$\mathcal{E}_{\Psi,A} := \{p(z_B), |\Psi_A(z_B)\rangle\} \quad (1)$$

Here, $\mathcal{E}_{\Psi,A}$ captures all information about the quantum many-body state $|\Psi\rangle$, superior to the reduced density matrix of A. In an infinite-temperature system without conserved charges, deep thermalization manifests as the emergence of a quantum state design (*12*–*15*), where a state k-design is an ensemble that reproduces the statistical properties of Haar-random states up to the kth moment. Accordingly, $\mathcal{E}_{\Psi,A}$ converges toward the Haar ensemble at long times (Fig. 1B).

Frequency-tunable superconducting qubits offer excellent controllability and have been widely used in quantum computation and simulation. However, conventional implementations rely on planar wiring, where the edge length scales unfavorably with increasing qubit number, limiting 2D scalability. Several efforts have been made to overcome the limitations of 2D scalability (*23*–*27*). However, achieving large-scale integration of frequency-tunable superconducting qubits remains challenging. Here, we implement a 3D-integrated architecture for frequency-tunable superconducting qubits, featuring a scalable packaging that uses pogo pins to ensure reliable electrical connectivity, achieving both high-fidelity control and scalable design (see Materials and Methods).

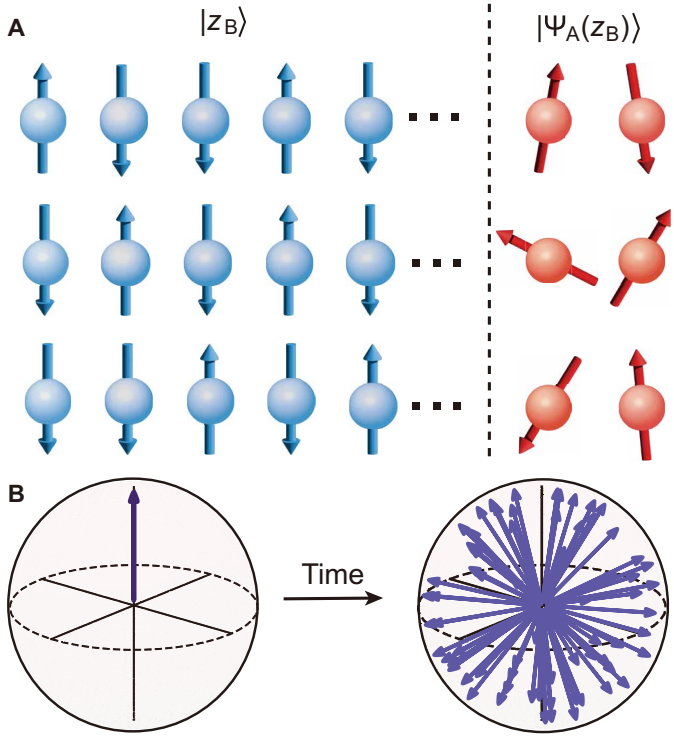

Fig. 1. Projected ensembles. (**A**) Schematic diagram of a projected ensemble. Red and blue spins represent subsystems A and B, respectively. Each projected result z_B corresponds to a measurement outcome $\Psi_A(z_B)$. (**B**) Sketch of deep thermalization. The system starts from a pure state, where the projected ensemble distributes on a local region of the Hilbert space. After a long-time evolution, the states of the projected ensemble distributes as a Haar ensemble, uniformly over the Hilbert space.

Our quantum processor consists of 16 concentric, frequency-tunable transmon qubits (*28*–*30*) arranged in a 4 × 4 square lattice (Fig. 2A). The qubits and readout circuits are patterned on the topside of the chip, while the contact pads for the control and readout ports are located on the backside. Each port is connected to a coaxial cable via a pogo pin that uses an internal spring to create a reliable electrical connection, enabling vertical wiring in a scalable manner. In addition, numerous superconductor-metalized through-silicon vias (TSVs) are placed across the chip. These TSVs have several crucial functions (see the Supplementary Materials for more details): connecting the ground planes on the topside and backside of the chip, localizing control and readout signals for cross-talk suppression, suppressing substrate modes, and functioning as transmission lines for the readout. The median energy-relaxation time T_1 of these qubits is 43 s, and the average readout fidelities are about 99.6 and 97.5% for states $|0\rangle$ and $|1\rangle$, respectively.

In the experiment, all qubits are tuned in resonance with each other during the time evolution. Thus, the effective Hamiltonian of this system can be described by a 2D spin-$\frac{1}{2}$ XY model (*31*–*33*), which is expressed as ($\hbar = 1$)

$$\hat{H} = \sum_{<i,j>} J_{ij}\left(\hat{\sigma}_i^+\hat{\sigma}_j^- + \text{h. c.}\right) \quad (2)$$

where $\hat{\sigma}^\alpha$ (for $\alpha \in \{x, y, z\}$) are the Pauli matrices, and the nearest-neighbor coupling J_{ij} is about $2\pi \times 4$ MHz (Fig. 2B). In the Supplementary Materials, the detailed parameters of the device are presented. The Hamiltonian $\hat{H}$ is a typical chaotic system with spin $U(1)$ symmetry (*22*, *34*, *35*), i.e., the total spin $\sum_j \hat{\sigma}_j^z$ is conserved.

Observation of deep thermalization

Here, we use projected ensembles to study deep thermalization. We select a half-filling state $|\Psi_0\rangle = |0101...01\rangle$ as the initial state. In this configuration, $\langle\Psi_0|\hat{H}|\Psi_0\rangle = 0$, corresponding to an infinite-temperature system. In addition, we select two bulk qubits, Q_5 and Q_6, as the subsystem A, while other qubits serve as subsystem B (Fig. 2B). In our experiment, we first prepare the initial state using single-qubit rotation gates on the target qubits and then bring all qubits into resonance. After a time t, the system evolves to the state $|\Psi(t)\rangle = e^{-i\hat{H}t/\hbar}|\Psi_0\rangle$. We lastly measure the relevant observables using joint single-shot readouts (Fig. 2C).

First, the ergodicity of the system is examined by monitoring a local observable, the density of qubit excitations $n_j := \langle\Psi(t)|\hat{\sigma}_j^+\hat{\sigma}_j^-|\Psi(t)\rangle$. As the system evolves, the distribution of n_j becomes homogeneous (Fig. 3A), which is a signature of conventional quantum thermalization. [Further details on the dynamics of n_j can be found in the Supplementary Materials (fig. S18).] Furthermore, we analyze the statistics of the bit string probability, $p(z) = |\langle z|\Psi(t)\rangle|^2$, where z is the outcome of the measurement bit-string of the entire system. To mitigate the decoherence effect, we only consider the half-filling sector by postselection. In Fig. 3B, we show the distributions of $p(z)$ at different evolution times. The results indicate that, for large t (but short compared with the coherence time), $p(z)$ follows the Porter-Thomas distribution $P(p) = \mathcal{D}e^{-\mathcal{D}p}$ (*34*, *36*–*38*), where $\mathcal{D} = 12{,}870$ is the dimension of the Hilbert space. We also consider the statistics of the measured conditional probability of subsystem A (*12*), written as $p(z_A|z_B)$. The experimental results show that $p(z_A = 10|z_B)$

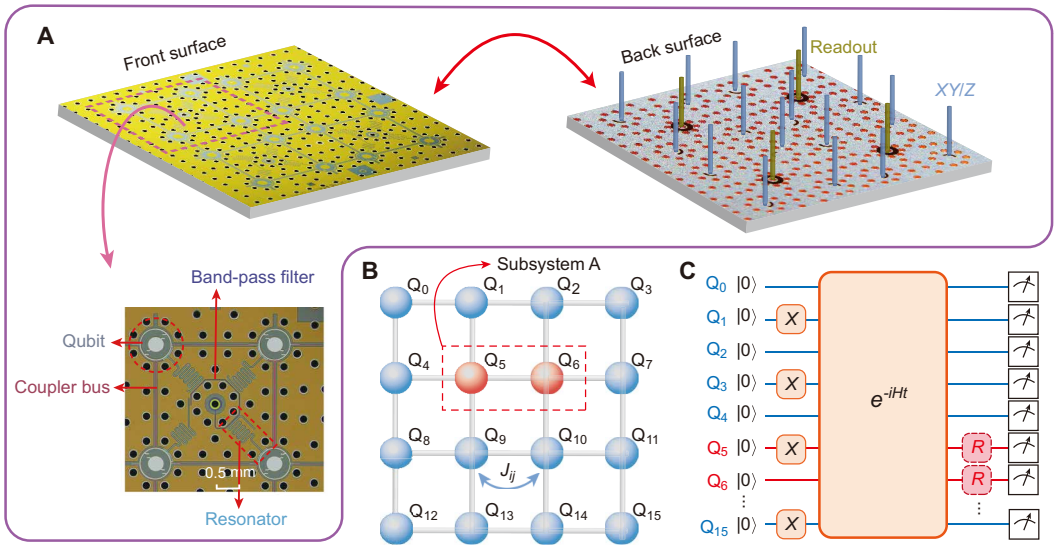

Fig. 2. Experimental setup. (**A**) Optical images with false color of the front and back sides of the 16-qubit superconducting chip. Control circuits, located on the back surface of the chip, are interconnected through pogo pins (blue and gray pins) to facilitate vertical wiring. Qubits and couplers are patterned on the front surface of the chip. The bottom false-colored image covers a single unit cell on the front side. Each unit (pink dashed box) involves four qubits, with each qubit being coupled to a λ/4 readout resonator (light blue). These four readout resonators are then coupled to the bandpass filter (purple). Neighboring two qubits are coupled capacitively via a coupler bus (red). The black holes are superconducting TSVs. The TSV located at the center of each unit is connected to a readout port backside and is coupled capacitively to the λ/4 band-pass filter at the front. (**B**) Effective lattice model of the experimental system. There are 16 qubits arranged in a 4 × 4 square lattice with nearest-neighbor spin-exchange interaction. The subsystem *A* contains two qubits: Q_5 and Q_6. (**C**) Experimental procedure. The initial state is prepared with *X* gates on the target qubits. Then, all qubits are tuned into resonance, and the system evolves under the Hamiltonian $\hat{H}$. After a time *t*, we perform a joint single-shot readout on all qubits. The dashed boxes *R* are the identity, *X*/2, or *Y*/2 gate, to realize state tomography.

exhibits a uniform distribution for a large t (Fig. 3C), where the deviation near the edges originates from decoherence (*12*). These results indicate that the steady state is well described by a random state, indicating the ergodicity of the system.

To study deep thermalization, we also need to consider projected ensembles. The projected ensemble of $|\Psi(t)\rangle$ is measured using joint measurements with single-shot readout (Fig. 2C). For subsystem B, the measurement is performed on the z-basis with outcomes z_B. For the two-qubit subsystem A (Q_5 and Q_6), we perform quantum state tomography by applying appropriate rotation gates to adjust the measurement basis before readout (Materials and Methods). Because of the conservation of total spin, the projected state $|\Psi_A(z_B)\rangle$ is the eigenstate of $(\hat{\sigma}_5^z+\hat{\sigma}_6^z)$, which prevents the projected ensemble $\mathcal{E}_{\Psi(t),A}$ from forming a Haar distribution. However, we can focus on the half-filling sector of the projected ensembles

$$\mathcal{E}^{\mathrm{hf}}_{\Psi(t),A} := \left\{ p\left[z_B \,|_{n(z_B)=7}\right], |\Psi_A(t,z_B)\rangle \right\} \tag{3}$$

where $n(z_B)$ denotes the total excitations in z_B. In this scenario, the output state of subsystem A is given by $|\Psi_A(t,z_B)\rangle = \alpha(t,z_B)|01\rangle + \beta(t,z_B)|10\rangle$. Thus, if $\mathcal{E}^{\mathrm{hf}}_{\Psi,A}$ approaches a Haar ensemble, it indicates that deep thermalization has occurred in this $U(1)$-symmetric system (*15*).

Owing to the system's coupling with the environment, the output states $|\Psi_A(t,z_B)\rangle$ are often mixed and may have nonzero components in the $|00\rangle$ and $|11\rangle$ bases. Therefore, we use the density matrices $\hat{\rho}_A(t,z_B)$ obtained by state tomography instead of $|\Psi_A(t,z_B)\rangle$. To further mitigate the impact of noise, we perform postselection by projecting $\hat{\rho}_A(t,z_B)$ onto the subspace spanned by $|01\rangle$ and $|10\rangle$ as

$$\tilde{\rho}_A(t,z_B) = \frac{\hat{\Pi}\hat{\rho}_A(t,z_B)\hat{\Pi}}{\mathrm{Tr}\left[\hat{\Pi}\hat{\rho}_A(t,z_B)\hat{\Pi}\right]} \tag{4}$$

where $\hat{\Pi} = |01\rangle\langle 01| + |10\rangle\langle 10|$. The distributions of $\tilde{\rho}_A(t,z_B)$ on the Bloch sphere are shown in Fig. 4A. At early times, $\tilde{\rho}_A(t,z_B)$ is primarily concentrated in a localized region. As the system evolves, $\tilde{\rho}_A(t,z_B)$ gradually delocalizes, and then becomes nearly uniform over the Bloch sphere. [The distributions of purity for each state $\tilde{\rho}_A(z_B)$ can be found in the Supplementary Materials (fig. S19).] This provides strong evidence that $\mathcal{E}^{\mathrm{hf}}_{\Psi(t),A}$ approximates a Haar ensemble after a sufficiently long time evolution, giving more information beyond the fact that the long-time state of subsystem A is a completely mixed state.

We also introduce the kth-moment density matrix (*12*–*14*) of $\mathcal{E}^{\mathrm{hf}}_{\Psi(t),A}$ as

$$\tilde{\rho}_A^{(k)}(t) = \sum_{z_B} p(z_B)\left[\tilde{\rho}_A(z_B)\right]^{\otimes k} \tag{5}$$

where $\tilde{\rho}_A^{(1)}$ is the density matrix of subsystem A. Generally, two ensembles are considered equivalent if their kth-moment density matrices are identical for any k. In Fig. 4B, we present the density matrices $\tilde{\rho}_A^{(2)}$ and $\tilde{\rho}_A^{(3)}$ at $t = 306$ ns, which approximate the corresponding kth-moment density matrices of the Haar ensemble. In the Supplementary Materials (fig. S20), we also present the corresponding experimental results of the kth-moment density matrices without postselection.

To quantitatively evaluate the distance between $\mathcal{E}^{\mathrm{hf}}_{\Psi(t),A}$ and the Haar ensemble, we define the trace distance between the kth-moment density matrix of $\mathcal{E}^{\mathrm{hf}}_{\Psi(t),A}$ and that of the Haar ensemble

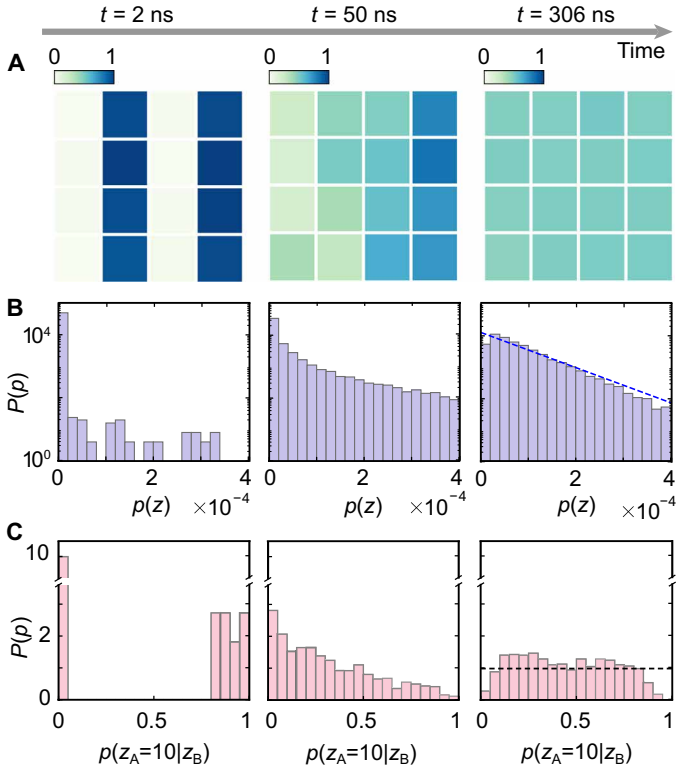

Fig. 3. Experimental signatures of ergodicity. (**A**) Distributions of the qubit excitations n_j for evolution times t = 2, 50, and 306 ns. (**B**) Statistics of the bit-string probability $p(z)$ for the different evolution times. The blue dashed line denotes an exponential fitting $P(p) = \mathcal{D}e^{-\mathcal{D}p}$, representing the Porter-Thomas distribution. (**C**) Distributions of the conditional probability $p(z_A = 10 \,|\, z_B)$ for different evolution times. The black dashed horizontal line denotes the uniform distribution.

$$\Delta^{(k)} := \frac{1}{2}\left\|\tilde{\rho}_A^{(k)} - \hat{\rho}_{Haar}^{(k)}\right\| \tag{6}$$

where $\|\cdot\|$ is the trace norm. As shown in Fig. 4C, $\Delta^{(k)}$ ($k = 1, 2, 3, 4$) approaches a small value after a long time $t \gtrsim 100$ ns, providing direct experimental evidence of deep thermalization. Note that $\Delta^{(k)}$ does not vanish completely due to finite-size effects and intrinsic noise [see numerical results in the Supplementary Materials (fig. S21)], and the dip at around 110 ns results from the competition between the thermalization and decoherence.

We now turn to the impact of noise on deep thermalization. The inherent coupling between the system and its environment can degrade the purity of quantum states, thereby altering the distribution of projected ensembles. To quantify this effect, we introduce the entropy of the kth-moment density matrix, defined as

$$S_A^{(k)} := \mathrm{Tr}\left[\tilde{\rho}_A^{(k)} \ln \tilde{\rho}_A^{(k)}\right] \tag{7}$$

If the entire system is in a pure state, we have $S_A^{(k)} \leq \ln(k+1)$, with equality holding for a Haar ensemble. As shown in Fig. 4D, when $k > 1$, the value of $S_A^{(k)}$ goes beyond $\ln(k+1)$ after a certain evolution time ($t \gtrsim 100$ ns), indicating that the state of the entire system becomes mixed. Thus, coupling with the environment prevents the projected ensemble from fully approaching a Haar ensemble. Nevertheless, Fig. 4D also demonstrates that the higher-order moments of the projected ensemble are highly sensitive to purity, suggesting their potential utility in detecting information leakage for the system to its environment.

Benchmarking many-body information leakage

Understanding environment-induced quantum purity decay and relaxation is essential for the development of quantum computation

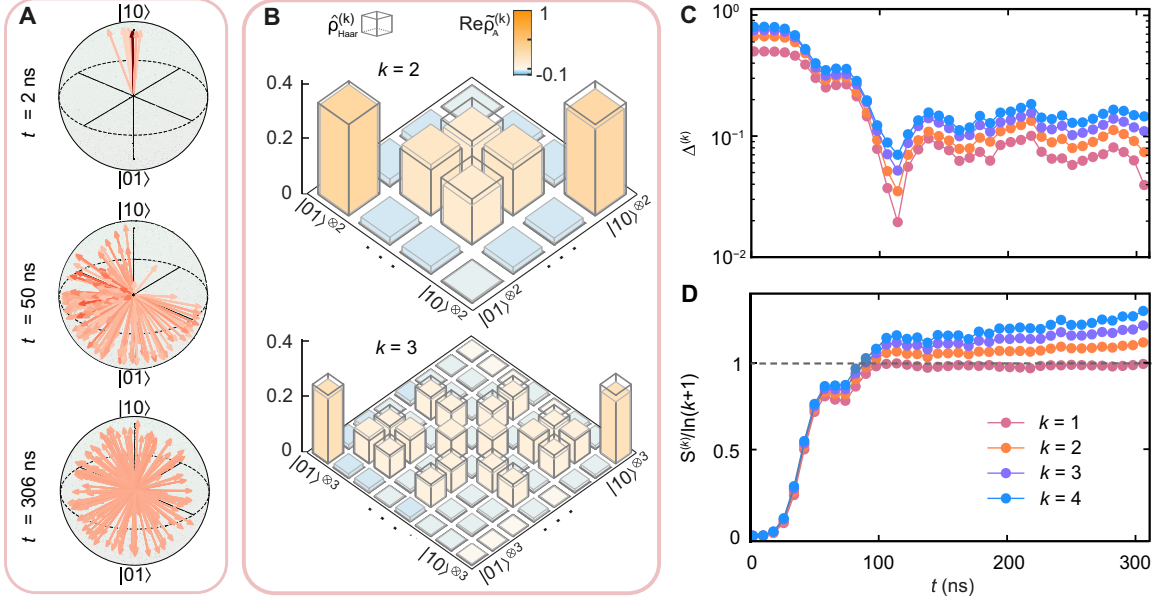

Fig. 4. Experimental signatures of deep thermalization. (**A**) Distributions of $\tilde{\rho}_A(z_B)$ on the Bloch sphere for t = 2, 50, and 306 ns. The north and south pole denote the states $|10\rangle$ and $|01\rangle$, respectively. The intensity of arrows' color is proportional to the probability $p(z_B)$. (**B**) Real parts of the second- and third-moment density matrices of $\mathcal{E}_{\Psi,A}^{hf}$ at t = 306 ns. The empty boxes are the corresponding density matrices of the Haar ensemble. (**C**) Dynamics of the trace distance $\Delta^{(k)}$ between the kth-moment density matrices ($k = 1, 2, 3, 4$) of $\mathcal{E}_{\Psi,A}^{hf}$ and the Haar ensemble. (**D**) Dynamics of $S_A^{(k)}/\ln(k+1)$, which is the normalized entropy of $\tilde{\rho}_A^{(k)}$.

and quantum simulation (*39*). However, conventional purity measures are difficult to apply in large-scale quantum simulators. Therefore, it is crucial to develop scalable approaches for quantifying many-body information leakage. We have shown that projected ensembles can capture purity of quantum many-body wave functions, making them a promising tool for assessing many-body information leakage.

We now use projected ensembles to benchmark many-body information leakage. For a projected ensemble $\mathcal{E}_{\Psi,\mathrm{A}}$, the information leakage makes a state $\hat{\rho}_{\mathrm{A}}(z_{\mathrm{B}})$ become mixed. Intuitively, as entropy of the entire system increases, the purity of states in $\mathcal{E}_{\Psi,\mathrm{A}}$ decreases. To quantify this, we introduce an ensemble-averaged entropy, defined as

$$\overline{E}_A = -\sum_{z_{\mathrm{B}}} p(z_{\mathrm{B}}) \ln \mathrm{Tr}\hat{\rho}_{\mathrm{A}}^2(z_{\mathrm{B}}) \tag{8}$$

A larger $\overline{E}_{\mathrm{A}}$ indicates a lower purity of the system and a larger information leakage to the environment. In the Supplementary Materials, we demonstrate that $\overline{E}_{\mathrm{A}}$ is generally proportional to the entropy of the entire system for small information leakage. In this case, $\overline{E}_{\mathrm{A}}$ can be approximated by a linear function (Materials and Methods)

$$\overline{E}_{\mathrm{A}} \approx E_0 \frac{t}{\tau_{\mathrm{MB}}} \tag{9}$$

where E_0 represents the steady-state value of $\overline{E}_{\mathrm{A}}$, and τ_{MB} serves as a decoherence time of the quantum many-body system, characterizing the speed of information leakage.

We first consider a 3×3 qubit system, and the central qubit (Q_6) is chosen as subsystem A (inset of Fig. 5A). The initial state is prepared as $|\psi_1\rangle = \otimes_{j=\mathrm{even}}|X_+\rangle \otimes_{j=\mathrm{odd}}|Y_+\rangle$, where $|X_+\rangle$ and $|Y_+\rangle$ are the eigenstates of $\hat{\sigma}^x$ and $\hat{\sigma}^y$, respectively, with eigenvalue +1. In this system, T_1 is much longer than both T_2^* and the evolution time, indicating that the effect of T_1 can be neglected. The sources for dephasing can generally be categorized into two types: white noise and $1/f$ noise (*40*). To study their effects, we perform numerical simulations of $\overline{E}_{\mathrm{A}}$ under white and $1/f$ noise, respectively, using the measured T_2^* values at the operation point. The experimental and numerical results for $\overline{E}_{\mathrm{A}}$ are compared in Fig. 5A. By fitting the experimental results with Eq. 9 ($E_0 = \ln 2$), we extract a lifetime of $\tau_{\mathrm{MB}} = 0.94 \pm 0.02$ μs (the observed offset may result from this initial state's sensitivity to dephasing noise during the Z-pulse tuning from the idle to the operation point), while the numerical predictions yield lifetimes of 0.353 ± 0.004 μs and 4.53 ± 0.04 μs for white noise and $1/f$ noise, respectively. Now, we consider the average single-qubit dephasing time (Materials and Methods), which can be defined as $\overline{T}_2^* = N / \left(\sum_{j=1}^{N} 1/T_{2,j}^* \right)$, where $T_{2,j}^*$ is the dephasing time of Q_j. For this nine-qubit system, we obtain $\overline{T}_2^* \approx 1.09$ μs, which is larger than the measured many-body decoherence time τ_{MB}.

Our numerical results indicate that $1/f$ noise leads to less information leakage compared to white noise, suggesting that quantum many-body systems are less sensitive to $1/f$ noise. This can be understood as follows: $1/f$ noise is the dominant source of dephasing in superconducting qubits (*30*, *41*, *42*). When all qubits are tuned to be resonant, their rapid coherent dynamics effectively averages out the low-frequency fluctuations of $1/f$ noise, thereby suppressing decoherence—a mechanism reminiscent of motional narrowing in nuclear magnetic resonance systems. However, in multiqubit superconducting circuits, additional nonnegligible noise sources may exist, such as leakage to higher excited states or coupling to spurious two-level systems. As a result, the experimentally observed lifetime falls between the lifetimes predicted for white noise and $1/f$ noise, reflecting the combined influence of various noise channels.

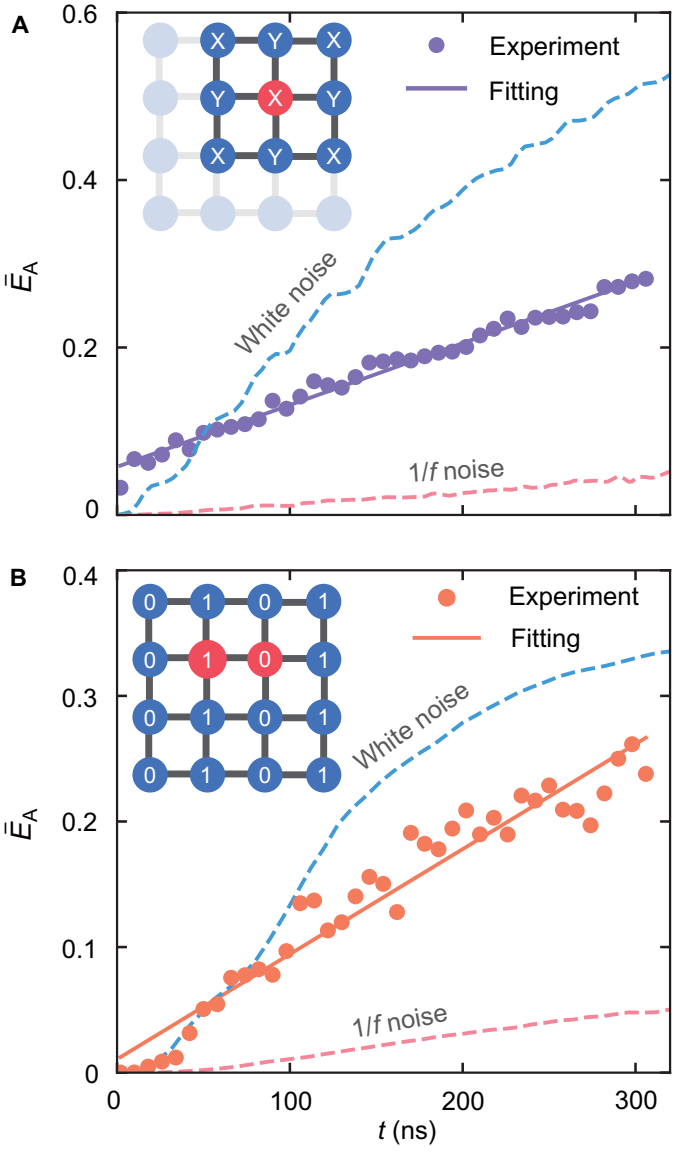

Fig. 5. Benchmark of many-body information leakage. (**A**) Dynamics of the averaged entropy $\overline{E}_{\mathrm{A}}$ of the projected ensembles for a 9-qubit system. The inset shows the system and the initial state. The red and blue qubits are subsystems A and B, respectively, and *X* (*Y*) corresponds to the initial states being the eigenstate of $\hat{\sigma}^x$ ($\hat{\sigma}^y$) with the positive eigenvalue. (**B**) Dynamics of the averaged entropy $\overline{E}_{\mathrm{A}}$ with spin-conserved initial states for a 16-qubit system. We consider all charge-conserved sectors of projected ensembles. The system structures and the initial states are also shown in the insets. The solid curves are linear fits. The dashed curves are numerical results with white and $1/f$ noise, respectively, performed using the QuTiP package (*53*).

We further extend our analysis to a 16-qubit system with spin-conserving, half-filling initial states (Fig. 5B). The experimentally observed $\overline{E}_{\mathrm{A}}$ again shows a linear increase at early times and lies between the numerical predictions for white and $1/f$ noise. These findings are consistent with those in the spin-nonconserving case (Fig. 5A).

DISCUSSION

In summary, we have experimentally explored deep thermalization and benchmarked many-body information leakage using projected ensembles on a 3D-integrated frequency-tunable superconducting quantum processor. Our results provide a direct experimental observation for the existence of deep thermalization. Moreover, we demonstrate that ensemble-averaged entropies can effectively quantify the extent of information leakage from a quantum many-body system to its environment. Our benchmark results reveal that single-qubit dephasing models are insufficient to fully capture the nature of information leakage in quantum many-body systems, due to the varying sensitivities to different types of noise. Therefore, using $\overline{E}_A$ as a benchmark for many-body information leakage is crucial for evaluating the performance of noisy quantum simulators.

Our findings demonstrate that projected ensembles offer a powerful approach for probing quantum many-body dynamics, providing complementary insights that go beyond those accessible through conventional density-matrix-based observables. Moreover, our benchmark method holds potential for advancing quantum computation and simulation. The scaling limitation can be mitigated by partitioning the system into multiple medium-sized blocks and detecting the information leakage within each block individually. This strategy can still offer insights beyond what single-qubit analyses can provide, enabling a more comprehensive characterization of noise-induced effects in large quantum systems.

Because projected ensembles can capture global information of quantum many-body wave functions, they may find broader applications in deepening our understanding of other areas of quantum many-body physics, including topological phases (*43*, *44*), and entanglement phases (*45*). Another promising application of projected ensembles in the context of open quantum systems (*39*) lies in characterizing information flow and non-Markovianity (*46*). Conventional measures of these phenomena, such as entanglement or trace distance (*47*–*49*), are difficult to scale to many-body regimes. In contrast, projected ensembles provide a practical alternative, making it a valuable tool for probing the non-Markovian dynamics and information backflow in open quantum many-body systems.

MATERIALS AND METHODS

Experimental setup

Our experiment is performed in a dilution refrigerator with a base temperature about 10 mK at the mixing-chamber stage. We use a scalable 3D-integrated superconducting quantum processor, which contains 16 qubits arranged in a 4×4 array (Fig. 2A). We implement a floating frequency-tunable transmon qubit with concentric and gradiometric geometry, optimized through the surface-participation-ratio analysis (*50*). The loop size of the concentric qubit is approximately $3 \times 10^5\ \mu m^2$.

Each qubit enables full controls (*XY* and *Z*), and the control signals access the qubits via spring contacts, featuring vertical wiring. In addition, we achieve the *X*–cross-talk below 1×10^{-3} and *Z*–cross-talk below 5×10^{-3} between any control port i and qubit Q_j ($i \neq j$). With the gradiometric geometry and optimized widths of the electrodes, the qubit $1/f$ flux noise is about $4.9\ \mu\Phi_0/\sqrt{\text{Hz}}$ at 1 Hz.

For readout, a band-pass filter (*51*) is used to indirectly couple the readout resonators to the transmission line, achieving an average qubit-resonator coupling strength of approximately $2\pi \times 150$ MHz, while maintaining the Purcell limit for the qubit relaxation times longer than 1 ms. This allows us to achieve a high signal-to-noise ratio (SNR) for the readout, and the average simultaneous readout assignment fidelities are about 99.6% and 97.5% for the states $|0\rangle$ and $|1\rangle$, respectively.

The anharmonicity of the qubits ranges from −248 to −218 MHz, which is more than 40 times larger than the coupling strength between the neighboring qubits. Thus, our system is in the hard-core limit, which can be described by a 2D spin-$\frac{1}{2}$ XY model in Eq. 2. More details about our experimental setup are provided in the Supplementary Materials.

Measuring projected ensembles

To measure projected ensembles, joint measurements with single-shot readout of all qubits are required. Before readout, the measurement basis for subsystem A is adjusted by applying rotation gates R on the target qubits to perform quantum state tomography (Fig. 2C). For a two-qubit subsystem A, quantum state tomography involves nine measurement bases: {*XX*, *XY*, *XZ*, *YX*, *YY*, *YZ*, *ZX*, *ZY*, *ZZ*}. For each basis v_A, we collect $M(v_A)$ single-shot outcomes, represented as bit strings of 16 qubits, with the count of each bit string z denoted as m_z. Our system achieves high readout fidelities and low readout cross-talks. To further mitigate readout errors, we optimize the measurement results using an approximate readout transition matrix (*52*)

$$\mathbb{F} = \bigotimes_{j=1}^{N} \begin{bmatrix} F_{00}^{j} & 1-F_{11}^{j} \\ 1-F_{00}^{j} & F_{11}^{j} \end{bmatrix} \tag{10}$$

where N is the number of qubits, and $F_{00(11)}^{j}$ represents the readout fidelity of state $|0\rangle(|1\rangle)$ for Q_j. Using this matrix, the optimized count of measurements for a given bit string z is calculated as

$$\tilde{m}_z = \sum_{z'} \mathbb{F}_{z,z'} m_{z'} \tag{11}$$

Then, we determine the optimized number of measurements for each bit string z_B under a given basis v_A, labeled as $\tilde{m}_{z_B}(v_A)$. Only bit strings z_B satisfying $\tilde{m}_{z_B}(v_A) \geq 80$ for all bases v_A are considered. From the single-shot results, we estimate the corresponding density matrix $\hat{\rho}_A(z_B)$. The probability of measuring z_B is then calculated as

$$p(z_B) = \frac{\sum_{v_A} \tilde{m}_{z_B}(v_A)}{\sum_{v_A} M(v_A)} \tag{12}$$

This procedure allows for the reconstruction of the projected ensemble.

For the 9-qubit experiment, the number of readouts per basis, $M(v_A)$, is approximately 8×10^4. For the 16-qubit experiments (with charge-conserved initial states), $M(v_A)$ varies with the evolution time, increasing as the evolution progresses, where $M(v_A)$ ranges from 2×10^5 to 5×10^5.

Benchmarking many-body information leakage

In superconducting circuits, dephasing can be modeled by a time-dependent Hamiltonian

$$\hat{H}(t) = \hat{H} + \frac{1}{2} \sum_j \xi_j(t) \hat{\sigma}_j^z \tag{13}$$

$$\langle \xi_j(0)\xi_j(t) \rangle = \int_{-\infty}^{\infty} \frac{d\omega}{2\pi} S_j(\omega) e^{-i\omega t} \quad (14)$$

where $\xi_j(t)$ represents Gaussian fluctuations, and $S_j(\omega)$ denotes the noise spectral density. For white and $1/f$ noise, the spectral densities satisfy $S_j(\omega) = W_j$ and $S_j(\omega) = A_j / |\omega|$, respectively. In the numerical simulations, we first extract the noise intensities W_j and A_j from the experimentally measured T_2^* values at the operating point (see fig. S5). In the experiment, each measurement cycle takes approximately 600 s, and the total time required to measure a projected ensemble is 10^3 to 10^4 s. Thus, for the $1/f$ noise, the low- and high-frequency cutoffs are set to 1 mHz and 100 kHz, respectively. For the white noise, a high-frequency cutoff of 1 GHz is used. We then compute $\overline{E}_A$ by solving the Schrödinger equation governed by the Hamiltonian in Eq. 13. All simulations are performed using the QuTiP package (*53*).

We also discuss how to obtain the average single-qubit dephasing time. We need to first obtain the average coupling strength with the environment, defined as

$$\overline{\gamma} = \frac{1}{N} \sum_{j=1}^{N} \frac{1}{T_{2,j}^*} \quad (15)$$

where $T_{2,j}^*$ is the dephasing time of Q_j. Thus, the average dephasing time is given by $\overline{T}_2^* = 1/\overline{\gamma}$.

Supplementary Materials

The PDF file includes:

Supplementary Text S1 to S7
Table S1
Figs. S1 to S21
Legend for movie S1
Legend for file S1
References

Other Supplementary Material for this manuscript includes the following:

Movie S1
File S1

REFERENCES

1. A. Polkovnikov, K. Sengupta, A. Silva, M. Vengalattore, *Colloquium*: Nonequilibrium dynamics of closed interacting quantum systems. *Rev. Mod. Phys.* **83**, 863 (2011).
2. I. Buluta, F. Nori, Quantum simulators. *Science* **326**, 108–111 (2009).
3. A. Trabesinger, Quantum simulation. *Nat. Phys.* **8**, 263 (2012).
4. I. M. Georgescu, S. Ashhab, F. Nori, Quantum simulation. *Rev. Mod. Phys.* **86**, 153 (2014).
5. J. M. Deutsch, Quantum statistical mechanics in a closed system. *Phys. Rev. A* **43**, 2046–2049 (1991).
6. M. Srednicki, Chaos and quantum thermalization. *Phys. Rev. E* **50**, 888–901 (1994).
7. M. Srednicki, The approach to thermal equilibrium in quantized chaotic systems. *J. Phys. A Math. Gen.* **32**, 1163 (1999).
8. M. Rigol, V. Dunjko, M. Olshanii, Thermalization and its mechanism for generic isolated quantum systems. *Nature* **452**, 854–858 (2008).
9. C. Neill, P. Roushan, M. Fang, Y. Chen, M. Kolodrubetz, Z. Chen, A. Megrant, R. Barends, B. Campbell, B. Chiaro, A. Dunsworth, E. Jeffrey, J. Kelly, J. Mutus, P. J. J. O'Malley, C. Quintana, D. Sank, A. Vainsencher, J. Wenner, T. C. White, A. Polkovnikov, J. M. Martinis, Ergodic dynamics and thermalization in an isolated quantum system. *Nat. Phys.* **12**, 1037 (2016).
10. A. M. Kaufman, M. E. Tai, A. Lukin, M. Rispoli, R. Schittko, P. M. Preiss, M. Greiner, Quantum thermalization through entanglement in an isolated many-body system. *Science* **353**, 794–800 (2016).
11. L. D'Alessio, Y. Kafri, A. Polkovnikov, M. Rigol, From quantum chaos and eigenstate thermalization to statistical mechanics and thermodynamics. *Adv. Phys.* **65**, 239–362 (2016).
12. J. Choi, A. L. Shaw, I. S. Madjarov, X. Xie, R. Finkelstein, J. P. Covey, J. S. Cotler, D. K. Mark, H.-Y. Huang, A. Kale, H. Pichler, F. G. S. L. Brandão, S. Choi, M. Endres, Preparing random states and benchmarking with many-body quantum chaos. *Nature* **613**, 468–473 (2023).
13. W. W. Ho, S. Choi, Exact emergent quantum state designs from quantum chaotic dynamics. *Phys. Rev. Lett.* **128**, 060601 (2022).
14. J. S. Cotler, D. K. Mark, H.-Y. Huang, F. Hernández, J. Choi, A. L. Shaw, M. Endres, S. Choi, Emergent quantum state designs from individual many-body wave functions. *PRX Quantum* **4**, 010311 (2023).
15. D. K. Mark, F. Surace, A. Elben, A. L. Shaw, J. Choi, G. Refael, M. Endres, S. Choi, Maximum entropy principle in deep thermalization and in Hilbert-space ergodicity. *Phys. Rev. X* **14**, 041051 (2024).
16. J. M. Renes, R. Blume-Kohout, A. J. Scott, C. M. Caves, Symmetric informationally complete quantum measurements. *J. Math. Phys.* **45**, 2171–2180 (2004).
17. A. Ambainis, J. Emerson, in *Twenty-Second Annual IEEE Conference on Computational Complexity (CCC'07)* (IEEE, 2007), pp. 129–140.
18. D. V. Averin, K. Xu, Y. P. Zhong, C. Song, H. Wang, S. Han, Suppression of dephasing by qubit motion in superconducting circuits. *Phys. Rev. Lett.* **116**, 010501 (2016).
19. K. Xu, J.-J. Chen, Y. Zeng, Y.-R. Zhang, C. Song, W. Liu, Q. Guo, P. Zhang, D. Xu, H. Deng, K. Huang, H. Wang, X. Zhu, D. Zheng, H. Fan, Emulating many-body localization with a superconducting quantum processor. *Phys. Rev. Lett.* **120**, 050507 (2018).
20. T. Brydges, A. Elben, P. Jurcevic, B. Vermersch, C. Maier, B. P. Lanyon, P. Zoller, R. Blatt, C. F. Roos, Probing Rényi entanglement entropy via randomized measurements. *Science* **364**, 260–263 (2019).
21. Google Quantum AI and Collaborators, Measurement-induced entanglement and teleportation on a noisy quantum processor. *Nature* **622**, 481–486 (2023).
22. A. H. Karamlou, I. T. Rosen, S. E. Muschinske, C. N. Barrett, A. Di Paolo, L. Ding, P. M. Harrington, M. Hays, R. Das, D. K. Kim, B. M. Niedzielski, M. Schuldt, K. Serniak, M. E. Schwartz, J. L. Yoder, S. Gustavsson, Y. Yanay, J. A. Grover, W. D. Oliver, Probing entanglement in a 2D hard-core Bose-Hubbard lattice. *Nature* **629**, 561–566 (2024).
23. J. Béjanin, T. McConkey, J. Rinehart, C. Earnest, C. McRae, D. Shiri, J. Bateman, Y. Rohanizadegan, B. Penava, P. Breul, S. Royak, M. Zapatka, A. G. Fowler, M. Mariantoni, Three-dimensional wiring for extensible quantum computing: The quantum socket. *Phys. Rev. Appl.* **6**, 044010 (2016).
24. J. Rahamim, T. Behrle, M. Peterer, A. Patterson, P. Spring, T. Tsunoda, R. Manenti, G. Tancredi, P. Leek, Double-sided coaxial circuit QED with out-of-plane wiring. *Appl. Phys. Lett.* **110**, 222602 (2017).
25. D. Rosenberg, D. Kim, R. Das, D. Yost, S. Gustavsson, D. Hover, P. Krantz, A. Melville, L. Racz, G. Samach, S. J. Weber, F. Yan, J. L. Yoder, A. J. Kerman, W. D. Oliver, 3D integrated superconducting qubits. *npj Quantum Inf.* **3**, 42 (2017).
26. D.-R. W. Yost, M. E. Schwartz, J. Mallek, D. Rosenberg, C. Stull, J. L. Yoder, G. Calusine, M. Cook, R. Das, A. L. Day, E. B. Golden, D. K. Kim, A. Melville, B. M. Niedzielski, W. Woods, A. J. Kerman, W. D. Oliver, Solid-state qubits integrated with superconducting through-silicon vias. *npj Quantum Inf.* **6**, 59 (2020).
27. P. A. Spring, S. Cao, T. Tsunoda, G. Campanaro, S. Fasciati, J. Wills, M. Bakr, V. Chidambaram, B. Shteynas, L. Carpenter, P. Gow, J. Gates, B. Vlastakis, P. J. Leek, High coherence and low cross-talk in a tileable 3D integrated superconducting circuit architecture. *Sci. Adv.* **8**, eabl6698 (2022).
28. J. Koch, T. M. Yu, J. Gambetta, A. A. Houck, D. I. Schuster, J. Majer, A. Blais, M. H. Devoret, S. M. Girvin, R. J. Schoelkopf, Charge-insensitive qubit design derived from the Cooper pair box. *Phys. Rev. A* **76**, 042319 (2007).
29. M. Kjaergaard, M. E. Schwartz, J. Braumüller, P. Krantz, J. I.-J. Wang, S. Gustavsson, W. D. Oliver, Superconducting qubits: Current state of play. *Annu. Rev. Condens. Matter Phys.* **11**, 369–395 (2020).
30. I. Siddiqi, Engineering high-coherence superconducting qubits. *Nat. Rev. Mater.* **6**, 875–891 (2021).
31. P. Roushan, C. Neill, J. Tangpanitanon, V. M. Bastidas, A. Megrant, R. Barends, Y. Chen, Z. Chen, B. Chiaro, A. Dunsworth, A. Fowler, B. Foxen, M. Giustina, E. Jeffrey, J. Kelly, E. Lucero, J. Mutus, M. Neeley, C. Quintana, D. Sank, A. Vainsencher, J. Wenner, T. White, H. Neven, D. G. Angelakis, J. Martinis, Spectroscopic signatures of localization with interacting photons in superconducting qubits. *Science* **358**, 1175–1179 (2017).
32. Z. Yan, Y.-R. Zhang, M. Gong, Y. Wu, Y. Zheng, S. Li, C. Wang, F. Liang, J. Lin, Y. Xu, C. Guo, L. Sun, C. Z. Peng, K. Xia, H. Deng, H. Rong, J. Q. You, F. Nori, H. Fan, X. Zhu, J. W. Pan, Strongly correlated quantum walks with a 12-qubit superconducting processor. *Science* **364**, 753–756 (2019).
33. Y. Ye, Z.-Y. Ge, Y. Wu, S. Wang, M. Gong, Y.-R. Zhang, Q. Zhu, R. Yang, S. Li, F. Liang, J. Lin, Y. Xu, C. Guo, L. Sun, C. Cheng, N. Ma, Z. Y. Meng, H. Deng, H. Rong, C.-Y. Lu, C.-Z. Peng, H. Fan, X. Zhu, J.-W. Pan, Propagation and localization of collective excitations on a 24-qubit superconducting processor. *Phys. Rev. Lett.* **123**, 050502 (2019).
34. T. I. Andersen, N. Astrakhantsev, A. H. Karamlou, J. Berndtsson, J. Motruk, A. Szasz, J. A. Gross, A. Schuckert, T. Westerhout, Y. Zhang, E. Forati, D. Rossi, B. Kobrin, A. D. Paolo, A. R. Klots, I. Drozdov, V. Kurilovich, A. Petukhov, L. B. Ioffe, A. Elben, A. Rath, V. Vitale, B. Vermersch, R. Acharya, L. A. Beni, K. Anderson, M. Ansmann, F. Arute, K. Arya, A. Asfaw,

J. Atalaya, B. Ballard, J. C. Bardin, A. Bengtsson, A. Bilmes, G. Bortoli, A. Bourassa, J. Bovaird, L. Brill, M. Broughton, D. A. Browne, B. Buchea, B. B. Buckley, D. A. Buell, T. Burger, B. Burkett, N. Bushnell, A. Cabrera, J. Campero, H. S. Chang, Z. Chen, B. Chiaro, J. Claes, A. Y. Cleland, J. Cogan, R. Collins, P. Conner, W. Courtney, A. L. Crook, S. das, D. M. Debroy, L. Lorenzo, A. D. T. Barba, S. Demura, P. Donohoe, A. Dunsworth, C. Earle, A. Eickbusch, A. M. Elbag, M. Elzouka, C. Erickson, L. Faoro, R. Fatemi, V. S. Ferreira, L. F. Burgos, A. G. Fowler, B. Foxen, S. Ganjam, R. Gasca, W. Giang, C. Gidney, D. Gilboa, M. Giustina, R. Gosula, A. G. Dau, D. Graumann, A. Greene, S. Habegger, M. C. Hamilton, M. Hansen, M. P. Harrigan, S. D. Harrington, S. Heslin, P. Heu, G. Hill, M. R. Hoffmann, H. Y. Huang, T. Huang, A. Huff, W. J. Huggins, S. V. Isakov, E. Jeffrey, Z. Jiang, C. Jones, S. Jordan, C. Joshi, P. Juhas, D. Kafri, H. Kang, K. Kechedzhi, T. Khaire, T. Khattar, M. Khezri, M. Kieferová, S. Kim, A. Kitaev, P. Klimov, A. N. Korotkov, F. Kostritsa, J. M. Kreikebaum, D. Landhuis, B. W. Langley, P. Laptev, K. M. Lau, L. L. Guevel, J. Ledford, J. Lee, K. W. Lee, Y. D. Lensky, B. J. Lester, W. Y. Li, A. T. Lill, W. Liu, W. P. Livingston, A. Locharla, D. Lundahl, A. Lunt, S. Madhuk, A. Maloney, S. Mandrà, L. S. Martin, O. Martin, S. Martin, C. Maxfield, J. McClean, M. McEwen, S. Meeks, K. C. Miao, A. Mieszala, S. Molina, S. Montazeri, A. Morvan, R. Movassagh, C. Neill, A. Nersisyan, M. Newman, A. Nguyen, M. Nguyen, C. H. Ni, M. Y. Niu, W. D. Oliver, K. Ottosson, A. Pizzuto, R. Potter, O. Pritchard, L. P. Pryadko, C. Quintana, M. J. Reagor, D. M. Rhodes, G. Roberts, C. Rocque, E. Rosenberg, N. C. Rubin, N. Saei, K. Sankaragomathi, K. J. Satzinger, H. F. Schurkus, C. Schuster, M. J. Shearn, A. Shorter, N. Shutty, V. Shvarts, V. Sivak, J. Skruzny, S. Small, W. C. Smith, S. Springer, G. Sterling, J. Suchard, M. Szalay, A. Sztein, D. Thor, A. Torres, M. M. Torunbalci, A. Vaishnav, S. Vdovichev, B. Villalonga, C. V. Heidweiller, S. Waltman, S. X. Wang, T. White, K. Wong, B. W. K. Woo, C. Xing, Z. J. Yao, P. Yeh, B. Ying, J. Yoo, N. Yosri, G. Young, A. Zalcman, N. Zhu, N. Zobrist, H. Neven, R. Babbush, S. Boixo, J. Hilton, E. Lucero, A. Megrant, J. Kelly, Y. Chen, V. Smelyanskiy, G. Vidal, P. Roushan, A. M. Läuchli, D. A. Abanin, X. Mi, Thermalization and criticality on an analogue-digital quantum simulator. *Nature* **638**, 79–85 (2025).
35. B. Blain, G. Marchegiani, L. Amico, G. Catelani, Suppressing chaos with mixed superconducting-qubit devices. *Phys. Rev. Appl.* **24**, 014048 (2025).
36. C. E. Porter, R. G. Thomas, Fluctuations of nuclear reaction widths. *Phys. Rev.* **104**, 483 (1956).
37. F. Arute, K. Arya, R. Babbush, D. Bacon, J. C. Bardin, R. Barends, R. Biswas, S. Boixo, F. G. S. L. Brandao, D. A. Buell, B. Burkett, Y. Chen, Z. Chen, B. Chiaro, R. Collins, W. Courtney, A. Dunsworth, E. Farhi, B. Foxen, A. Fowler, C. Gidney, M. Giustina, R. Graff, K. Guerin, S. Habegger, M. P. Harrigan, M. J. Hartmann, A. Ho, M. Hoffmann, T. Huang, T. S. Humble, S. V. Isakov, E. Jeffrey, Z. Jiang, D. Kafri, K. Kechedzhi, J. Kelly, P. V. Klimov, S. Knysh, A. Korotkov, F. Kostritsa, D. Landhuis, M. Lindmark, E. Lucero, D. Lyakh, S. Mandra, J. R. McClean, M. McEwen, A. Megrant, X. Mi, K. Michielsen, M. Mohseni, J. Mutus, O. Naaman, M. Neeley, C. Neill, M. Y. Niu, E. Ostby, A. Petukhov, J. C. Platt, C. Quintana, E. G. Rieffel, P. Roushan, N. C. Rubin, D. Sank, K. J. Satzinger, V. Smelyanskiy, K. J. Sung, M. D. Trevithick, A. Vainsencher, B. Villalonga, T. White, Z. J. Yao, P. Yeh, A. Zalcman, H. Neven, J. M. Martinis, Quantum supremacy using a programmable superconducting processor. *Nature* **574**, 505–510 (2019).
38. T. Liu, S. Liu, H. Li, H. Li, K. Huang, Z. Xiang, X. Song, K. Xu, D. Zheng, H. Fan, Observation of entanglement transition of pseudo-random mixed states. *Nat. Commun.* **14**, 1971 (2023).
39. D. A. Lidar, Lecture notes on the theory of open quantum systems. arXiv:1902.00967 [quant-ph] (2019).
40. E. Paladino, Y. M. Galperin, G. Falci, B. L. Altshuler, 1/*f* noise: Implications for solid-state quantum information. *Rev. Mod. Phys.* **86**, 361 (2014).
41. F. Yoshihara, K. Harrabi, A. O. Niskanen, Y. Nakamura, J. S. Tsai, Decoherence of flux qubits due to 1/*f* flux noise. *Phys. Rev. Lett.* **97**, 167001 (2006).
42. R. McDermott, Materials origins of decoherence in superconducting qubits. *IEEE Trans. Appl. Supercond.* **19**, 2–13 (2009).
43. A. Kitaev, J. Preskill, Topological entanglement entropy. *Phys. Rev. Lett.* **96**, 110404 (2006).
44. X. Chen, Z.-C. Gu, X.-G. Wen, Local unitary transformation, long-range quantum entanglement, wave function renormalization, and topological order. *Phys. Rev. B* **82**, 155138 (2010).
45. Z.-Y. Ge, F. Nori, Identifying entanglement phases with bipartite projected ensembles. *Phys. Rev. Res.* **7**, 043022 (2025).
46. H.-P. Breuer, E.-M. Laine, J. Piilo, B. Vacchini, *Colloquium*: Non-Markovian dynamics in open quantum systems. *Rev. Mod. Phys.* **88**, 021002 (2016).
47. A. Rivas, S. F. Huelga, M. B. Plenio, Entanglement and non-markovianity of quantum evolutions. *Phys. Rev. Lett.* **105**, 050403 (2010).
48. X.-M. Lu, X. Wang, C. P. Sun, Quantum Fisher information flow and non-Markovian processes of open systems. *Phys. Rev. A* **82**, 042103 (2010).
49. Y.-N. Lu, Y.-R. Zhang, G.-Q. Liu, F. Nori, H. Fan, X.-Y. Pan, Observing information backflow from controllable non-Markovian multichannels in diamond. *Phys. Rev. Lett.* **124**, 210502 (2020).
50. C. Wang, C. Axline, Y. Y. Gao, T. Brecht, Y. Chu, L. Frunzio, M. Devoret, R. J. Schoelkopf, Surface participation and dielectric loss in superconducting qubits. *Appl. Phys. Lett.* **107**, 162601 (2015).
51. E. Jeffrey, D. Sank, J. Mutus, T. White, J. Kelly, R. Barends, Y. Chen, Z. Chen, B. Chiaro, A. Dunsworth, A. Megrant, P. J. O'Malley, C. Neill, P. Roushan, A. Vainsencher, J. Wenner, A. N. Cleland, J. M. Martinis, Fast accurate state measurement with superconducting qubits. *Phys. Rev. Lett.* **112**, 190504 (2014).
52. Y. Zheng, C. Song, M.-C. Chen, B. Xia, W. Liu, Q. Guo, L. Zhang, D. Xu, H. Deng, K. Huang, Y. Wu, Z. Yan, D. Zheng, L. Lu, J.-W. Pan, H. Wang, C.-Y. Lu, X. Zhu, Solving systems of linear equations with a superconducting quantum processor. *Phys. Rev. Lett.* **118**, 210504 (2017).
53. J. Johansson, P. Nation, F. Nori, QuTiP 2: A Python framework for the dynamics of open quantum systems. *Comput. Phys. Commun.* **184**, 1234–1240 (2013).
54. T. Roy, S. Kundu, M. Chand, A. Vadiraj, A. Ranadive, N. Nehra, M. P. Patankar, J. Aumentado, A. Clerk, R. Vijay, Broadband parametric amplification with impedance engineering: Beyond the gain-bandwidth product. *Appl. Phys. Lett.* **107**, 262601 (2015).
55. J. Braumüller, L. Ding, A. P. Vepsäläinen, Y. Sung, M. Kjaergaard, T. Menke, R. Winik, D. Kim, B. M. Niedzielski, A. Melville, J. L. Yoder, C. F. Hirjibehedin, T. P. Orlando, S. Gustavsson, W. D. Oliver, Characterizing and optimizing qubit coherence based on SQUID geometry. *Phys. Rev. Appl.* **13**, 054079 (2020).
56. S. Bravyi, D. P. DiVincenzo, D. Loss, Schrieffer–Wolff transformation for quantum many-body systems. *Ann. Phys.* **326**, 2793–2826 (2011).
57. A. Potts, P. Routley, G. J. Parker, J. Baumberg, P. De Groot, Novel fabrication methods for submicrometer Josephson junction qubits. *J. Mater. Sci. Mater. Electron.* **12**, 289–293 (2001).
58. L. DiCarlo, J. M. Chow, J. M. Gambetta, L. S. Bishop, B. R. Johnson, D. Schuster, J. Majer, A. Blais, L. Frunzio, S. Girvin, R. J. Schoelkopf, Demonstration of two-qubit algorithms with a superconducting quantum processor. *Nature* **460**, 240–244 (2009).
59. E. Magesan, J. M. Gambetta, J. Emerson, Scalable and robust randomized benchmarking of quantum processes. *Phys. Rev. Lett.* **106**, 180504 (2011).
60. J. M. Gambetta, A. D. Córcoles, S. T. Merkel, B. R. Johnson, J. A. Smolin, J. M. Chow, C. A. Ryan, C. Rigetti, S. Poletto, T. A. Ohki, M. B. Ketchen, M. Steffen, Characterization of addressability by simultaneous randomized benchmarking. *Phys. Rev. Lett.* **109**, 240504 (2012).
61. R. Barends, J. Kelly, A. Megrant, A. Veitia, D. Sank, E. Jeffrey, T. C. White, J. Mutus, A. G. Fowler, B. Campbell, Y. Chen, Z. Chen, B. Chiaro, A. Dunsworth, C. Neill, P. O'Malley, P. Roushan, A. Vainsencher, J. Wenner, A. N. Korotkov, A. N. Cleland, J. M. Martinis, Superconducting quantum circuits at the surface code threshold for fault tolerance. *Nature* **508**, 500–503 (2014).
62. E. A. Sete, J. M. Martinis, A. N. Korotkov, Quantum theory of a bandpass Purcell filter for qubit readout. *Phys. Rev. Appl.* **92**, 012325 (2015).
63. J. Gambetta, A. Blais, M. Boissonneault, A. A. Houck, D. Schuster, S. M. Girvin, Quantum trajectory approach to circuit QED: Quantum jumps and the Zeno effect. *Phys. Rev. A* **77**, 012112 (2008).
64. X. Jin, A. Kamal, A. Sears, T. Gudmundsen, D. Hover, J. Miloshi, R. Slattery, F. Yan, J. Yoder, T. Orlando, S. Gustavsson, W. D. Oliver, Thermal and residual excited-state population in a 3D transmon qubit. *Phys. Rev. Lett.* **114**, 240501 (2015).
65. M. A. Rol, L. Ciorciaro, F. K. Malinowski, B. M. Tarasinski, R. E. Sagastizabal, C. C. Bultink, Y. Salathe, N. Haandbæk, J. Sedivy, L. DiCarlo, Time-domain characterization and correction of on-chip distortion of control pulses in a quantum processor. *Appl. Phys. Lett.* **116**, 054001 (2020).
66. P. Klimov, J. Kelly, Z. Chen, M. Neeley, A. Megrant, B. Burkett, R. Barends, K. Arya, B. Chiaro, Y. Chen, A. Dunsworth, A. Fowler, B. Foxen, C. Gidney, M. Giustina, R. Graff, T. Huang, E. Jeffrey, E. Lucero, J. Y. Mutus, O. Naaman, C. Neill, C. Quintana, P. Roushan, D. Sank, A. Vainsencher, J. Wenner, T. C. White, S. Boixo, R. Babbush, V. N. Smelyanskiy, H. Neven, J. M. Martinis, Fluctuations of energy-relaxation times in superconducting qubits. *Phys. Rev. Lett.* **121**, 090502 (2018).
67. J. J. Burnett, A. Bengtsson, M. Scigliuzzo, D. Niepce, M. Kudra, P. Delsing, J. Bylander, Decoherence benchmarking of superconducting qubits. *npj Quantum Inf.* **5**, 54 (2019).
68. X.-Y. Guo, Z.-Y. Ge, H. Li, Z. Wang, Y.-R. Zhang, P. Song, Z. Xiang, X. Song, Y. Jin, L. Lu, K. Xu, D. Zheng, H. Fan, Observation of Bloch oscillations and Wannier-Stark localization on a superconducting quantum processor. *npj Quantum Inf.* **7**, 51 (2021).

Acknowledgments: We thank M. Dalmonte (ICTP, Italy), L. Glazman (Yale University, USA), and N. Astrakhantsev (Google Quantum AI, USA) for helpful discussions. **Funding:** Z.Y. and Y.N. are partially supported by the Ministry of Education, Culture, Sports, Science and Technology (MEXT) Quantum Leap Flagship Program (QLEAP) (via grant no. JPMXS0118068682). F.N. is supported in part by the Japan Science and Technology Agency (JST) (via the CREST Quantum Frontiers program grant no. JPMJCR24I2, the Moonshot R&D grant no. JPMJMS256E), and the Office of Naval Research (ONR) Global (via grant no. N62909-23-1-2074). Y.-R.Z. is supported in part by the National Natural Science Foundation of China (via grant no. 12475017) and the Natural Science Foundation of Guangdong Province (via grant no. 2024A1515010398). **Author contributions:** Z.Y., Z.-Y.G., F.N., and Y.N. conceived the idea and experiment. Z.Y. performed the experiments. Z.-Y.G. contributed to the underlying theory. Z.Y. improved the spring contacts for DC-bias, designed and fabricated the chip, and set up the measurement system. R.L. and Z.Y. developed the measurement code. Z.-Y.G. and Z.Y. performed data analysis and wrote the manuscript. Z.Y., Z.-Y.G., R.L., Y.-R.Z., F.N., and Y.N. contributed to revising the manuscript and the Supplementary

Materials. F.N. and Y.N. supervised this project. **Competing interests:** The authors declare that they have no competing interests. **Data, code, and materials availability:** All data and code needed to evaluate and reproduce the results in the paper are present in the paper and/or the Supplementary Materials. This study did not generate new materials.

Submitted 27 August 2025
Accepted 24 February 2026
Published 27 March 2026
10.1126/sciadv.aeb8213

ScienceAdvances

Characterizing many-body dynamics with projected ensembles on a superconducting quantum processor

Zhiguang Yan, Zi-Yong Ge, Rui Li, Yu-Ran Zhang, Franco Nori, and Yasunobu Nakamura

Sci. Adv. **12** (13), eaeb8213. DOI: 10.1126/sciadv.aeb8213

Science Advances (ISSN 2375-2548) is published by the American Association for the Advancement of Science. 1200 New York Avenue NW, Washington, DC 20005. The title *Science Advances* is a registered trademark of AAAS.